

High-Performance Ultraviolet Photodetector Based on Organic–Inorganic Hybrid Structure

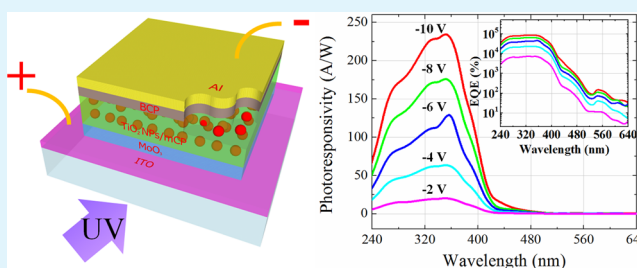
Dali Shao,[†] Mingpeng Yu,^{‡,§} Hongtao Sun,[‡] Guoqing Xin,[‡] Jie Lian,[‡] and Shayla Sawyer^{*,†}

[†]Department of Electrical, Computer, and Systems Engineering and [‡]Department of Mechanical, Aerospace and Nuclear Engineering, Rensselaer Polytechnic Institute, Troy, New York 12180, United States

[§]Department of Chemistry, Tsinghua University, Beijing 100084, China

ABSTRACT: An ultraviolet (UV) photodetector is fabricated by sandwiching a nanocomposite active layer between charge-selective semiconducting polymers. The nanocomposite active layer composed of TiO₂ nanoparticles (NPs) blended with 1,3-bis(*N*-carbazolyl)benzene (mCP), which acts as a “valve” controller that enables hole injection into the device upon UV illumination. The UV photodetector demonstrated a high photocurrent to dark current ratio ($\sim 10^4$), a large linear dynamic range of 60 dB, and a remarkable external quantum efficiency ($\sim 8.5 \times 10^4\%$) for the UV light at 351 nm. In addition to discussing the performance of the UV photodetector, a general strategy for design and fabrication of high-performance UV photodetectors with hole injection operation mode is suggested.

KEYWORDS: ultraviolet photodetector, organic–inorganic, TiO₂, polymer, photoresponsivity, hole injection



1. INTRODUCTION

UV photodetectors have been investigated for a wide range of applications, such as secure space-to-space communications, pollution monitoring, water sterilization, flame sensing, and early missile plume detection.^{1–3} To date, most of the commercial photodetectors are fabricated from single-crystalline silicon, silicon carbide, or gallium nitride p–n junction photodiodes. However, the responsivity of these inorganic photodetectors is low (< 0.2 A/W), and their fabrication process is usually complex.⁴ UV photodetectors fabricated from organic–inorganic composite materials may offer an inexpensive technology for manufacturing while at the same time achieve comparable or even higher sensitivity.^{5–7} In addition to the excellent performance of these organic–inorganic hybrid photodetectors, the energy band structures of organic–inorganic hybrid material systems can be easily manipulated by simply revising the molecule structure of the polymers, providing us unmatched design flexibility.^{8–10} Keeping these in mind, here we present a highly sensitive UV photodetector fabricated by sandwiching a mCP–TiO₂ NPs nanocomposite layer between charge-selective semiconducting polymers. The mCP–TiO₂ NPs nanocomposite layer acts as a “valve” controller that enables hole injection into the device upon UV illumination, which brings the UV photodetector with high photocurrent to dark current ratio and high photoresponsivity.

2. EXPERIMENTAL METHODS

All chemical reagents were purchased from Sigma-Aldrich and used without further purification. First, ammonium solution (8 wt %) was added dropwise into titanium trichloride solution under vigorous stirring until a white precipitate is obtained. The resulting suspension

was maintained at room temperature for 3 h and then filtered and thoroughly washed with deionized water and absolute ethanol several times to remove the remaining ammonium and chloride ions. Then, anatase TiO₂ NPs were obtained after transferring the wet as-prepared precipitation to an autoclave at 200 °C for 20 h.

The UV photodetector was fabricated on ITO glass substrates after cleaning by ultrasonication in acetone, detergent, water, and isopropanol and treatment in ultraviolet/ozone to remove carbon residues. First, a thin layer of MoO₃ with a thickness of approximately 5 nm was deposited onto the precleaned ITO glass substrate using thermal evaporation with a deposition rate at ~ 0.5 Å/s. MoO₃ acts as a hole transport/electron blocking layer.^{11,12} The photoactive layers were made of blends of TiO₂ NPs with mCP at a ratio of 3:1 by weight. The mCP–TiO₂ NPs blends were dispersed in toluene solvent (24 mg/mL) and spin coated on top of the MoO₃ layer to form the active layer of the device. The mCP–TiO₂ NPs composite layer has a thickness of around 300 nm. Afterward, a 20 nm thick bathocuproine (BCP) layer was deposited on top of the mCP–TiO₂ NPs photoactive layer using thermal evaporation. The BCP layer acts as an electron transport/hole blocking layer.^{13,14} Then, a top Al contact layer with a thickness of 175 nm was deposited via an electron beam evaporator using a shadow mask. Finally, the photodetector was packaged and wire bonded using Epo-Tek H20E conductive epoxy. Figure 1a shows the schematic illustration of the hybrid UV photodetector and the molecular structures of mCP and BCP. The energy band diagram of the device is presented in Figure 1b.

The Raman spectrum of the as-prepared TiO₂ NPs was measured using the Renishaw spectrometer with a laser wavelength of 514 nm (Renishaw, Wotton-under-Edge, UK). The X-ray diffraction (XRD, PANalytical) pattern was measured at room temperature with Cu K α

Received: June 24, 2014

Accepted: July 2, 2014

Published: July 2, 2014

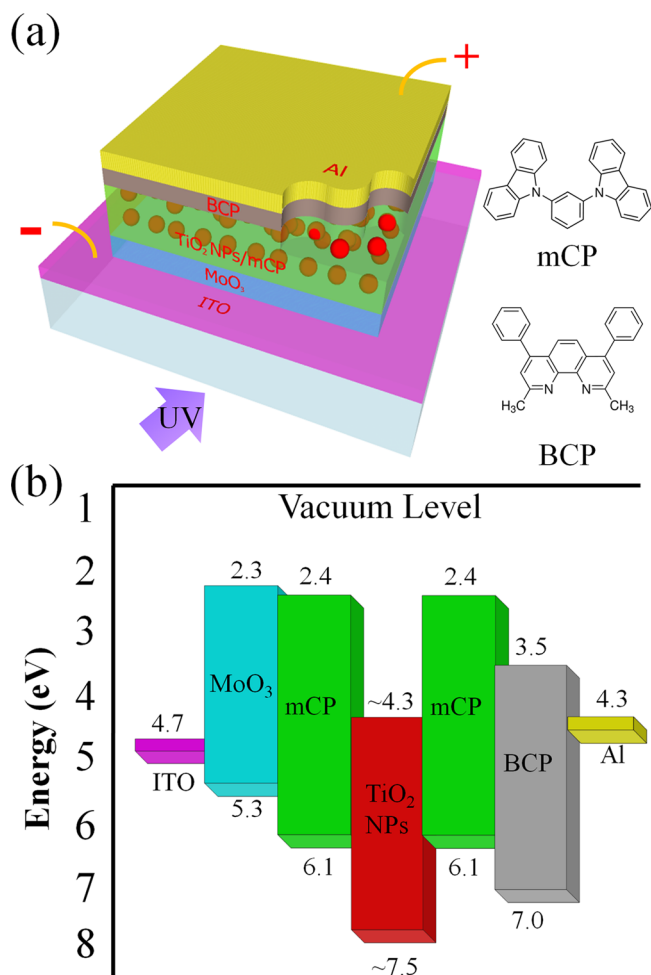


Figure 1. (a) Schematic illustration of the hybrid UV photodetector, and molecular structures of mCP and BCP. (b) Energy band diagram of the hybrid UV photodetector.

radiation (wavelength = 1.54 Å). The absorption spectrum of the mCP–TiO₂ composite layer was measured using a Shimadzu UV–vis 2550 spectrophotometer with a deuterium lamp (190–390 nm) and a halogen lamp (280–1100 nm). The typical *J*–*V* characteristics and transient response of the photodetector were measured using a HP4155B semiconductor parameter analyzer. The photoresponsivity of the photodetector was measured using a Shimadzu UV–vis 2550

spectrophotometer in connection with a Newport 1928-C optical power meter.

3. RESULTS AND DISCUSSION

Figure 2a shows the Raman spectrum of the TiO₂ NPs. The Raman peaks at 142, 195, 394, 514, and 636 cm⁻¹ can be assigned as E_g, E_g, B_{1g}, A_{1g}, and E_g modes of the anatase phase, respectively. The XRD pattern of the as-prepared TiO₂ NPs is shown in Figure 2b, in which nine peaks from the anatase structured TiO₂ can be well observed, confirming that the TiO₂ NPs is crystallized in the anatase structure. The UV–vis absorption spectrum of the mCP–TiO₂ active layer is shown in Figure 2c. It is clear from Figure 2c that the absorption spectrum of the mCP–TiO₂ active layer has two absorption edges located at around 330 and 370 nm, which are attributed to the absorption in TiO₂ NPs and mCP, respectively.

The typical *J*–*V* characteristics of this photodetector were measured in the dark and with 335 nm UV illumination, as shown in Figure 3. The dark current of the photodetector

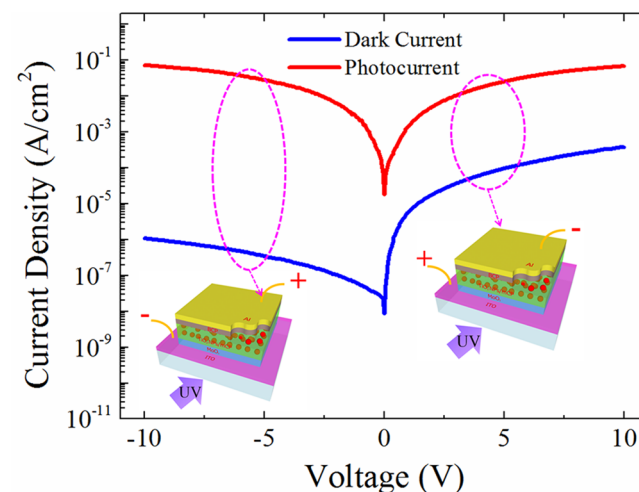


Figure 3. Typical *J*–*V* characteristics of the hybrid UV photodetector measured in the dark and with 335 nm UV illumination.

displayed a significant rectification characteristic with a rectification ratio of 292 when biased at ±5 V. The rectification characteristic of the photodetector under dark environment can be understood by referring to the energy band diagram in

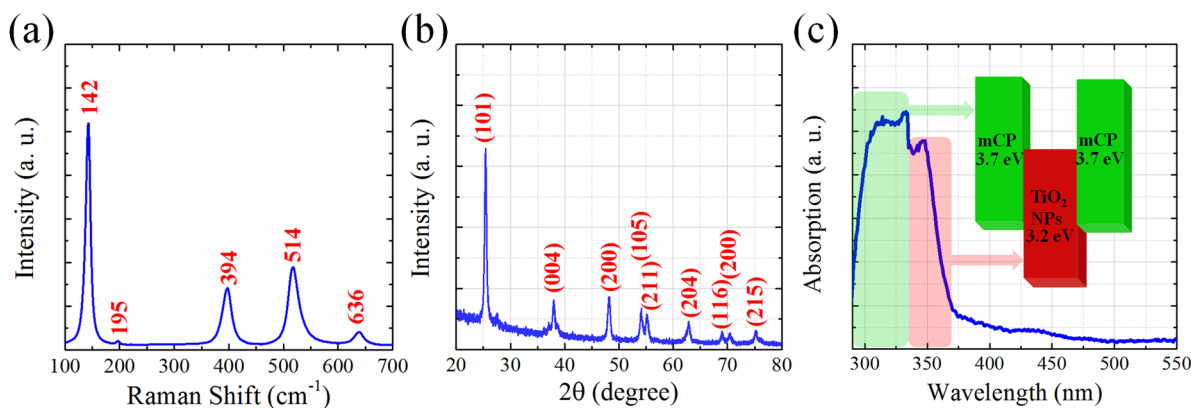


Figure 2. (a and b) Raman spectrum and XRD pattern of the as-prepared TiO₂ NPs, respectively. (c) Absorption spectrum of the mCP–TiO₂ composite layer.

Figure 4a. Under reverse bias condition, the BCP's hole blocking ability together with the large valence band offset

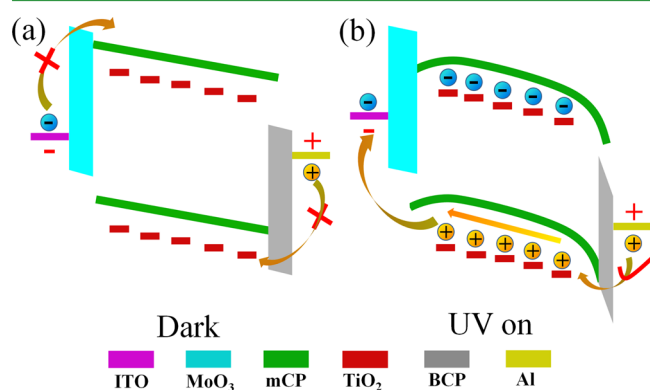


Figure 4. (a and b) Energy band diagram and carrier transport process of the hybrid UV photodetector in the dark and with UV illumination, respectively.

between BCP and Al can effectively impede hole injection from the Al contact. Similarly, electron injection from the ITO can be greatly suppressed due to MoO₃'s electron blocking ability together with the large conduction band offset between ITO and MoO₃. On the contrary, under forward bias condition, the electrons and holes can be injected from Al to BCP and from ITO to MoO₃, leading to higher dark current as compared to the reverse biased condition. Upon UV illumination, the photogenerated current is more than 4 orders of magnitude higher than the dark current when reverse biased. Such a high photocurrent to dark current ratio under reverse bias condition is due to injection of a large amount of holes from the top Al contact into the device. As illustrated in Figure 4b, both the TiO₂ NPs and mCP absorb incident photons and generate electron-hole pairs under UV illumination. The photogenerated holes in TiO₂ NPs can be transported through mCP and MoO₃ and finally be collected from ITO under external bias voltage. On the contrary, the photogenerated electrons remain trapped in the nanoparticles due to the lack of a percolation network for electrons and the strong quantum confinement effect of the mCP-TiO₂ NPs composite structure. The trapped electrons quickly shift the lowest unoccupied molecular orbital (LUMO) of the mCP downward and align the Fermi energy of the nanocomposite with that of the Al. Therefore, the hole-injection barrier on the Al side becomes very thin, and the holes can easily tunnel through it with a small reverse bias. Accordingly, the Al-BCP interface acts as a "valve" for hole injection that is controlled by the mCP-TiO₂ composite layer, and incident photons can switch on this "valve".

As the operation of this UV photodetector strongly depends on the electron trapping and hole injection in the mCP-TiO₂ layer, it is necessary to verify the electron-trapping capability and hole transport properties of the mCP-TiO₂ layer. Therefore, we fabricated and tested hole-only and electron-only devices. The electron-only and hole-only devices have structures of ITO/Cs₂CO₃/mCP-TiO₂/BCP/Al and ITO/MoO₃/mCP-TiO₂/MoO₃/Al, respectively. For the electron device, both the Cs₂CO₃ layer and the BCP layer are electron transport layers with the capability of blocking holes; therefore, only electrons can be injected. Similarly, MoO₃ has been demonstrated as an effective hole injection layer with good

capability of blocking electrons; therefore, only holes can be injected into the hole-only device. The results are shown in Figure 5, from which we can see that the current density in the

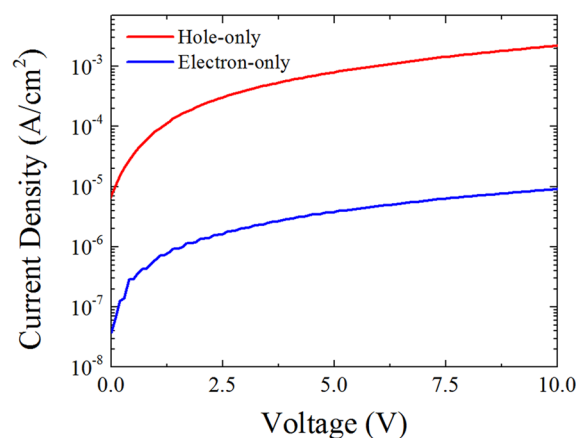


Figure 5. J - V curves of the electron-only and hole-only devices measured for verification of the carrier transport properties of the mCP-TiO₂ NPs composite.

hole-only device is more than 2 orders of magnitude higher than that of the electron-only device. This verifies that electrons can hardly move in the active layer due to the electron-trapping centers formed by TiO₂ NPs, while the holes can freely move in the device structure.

The room-temperature photoresponsivity spectra of the hybrid photodetector measured with varying external bias voltage is shown in Figure 6. A maximum photoresponsivity of

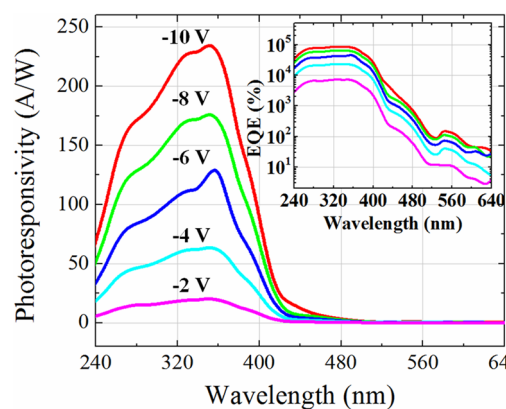


Figure 6. Photoresponsivity spectra of the hybrid UV photodetector measured with varying bias voltages. (Inset) Calculated EQE of the hybrid UV photodetector.

240 A/W at 351 nm was observed when reverse biased at -10 V, which is more than 3 orders of magnitude higher than those of commercial GaN or SiC photodetectors (<0.2 A/W).⁴ The inset of Figure 6 shows the EQE of the photodetector calculated using the equation $EQE = R \times hv/q$, where hv is the energy of the incident photon in electronvolts, q is the electron charge, and R is the photoresponsivity of the hybrid photodetector. A maximum EQE as high as $\sim 8.5 \times 10^4\%$ has been achieved for the UV light (351 nm). The high EQE is mainly attributed to the hole injection from the top contact that is controlled by the electron traps in the active region (mCP-TiO₂) of the hybrid UV photodetector. This operation

mechanism enables injection and collection of multiple holes by the electrode following a single electron–hole photogeneration in the active layer, leading to a high EQE.

In practical applications, a constant responsivity from strong light all the way down to weak light is important so that a photodetector can be applied for weak light sensing. Every photodetector only has a finite range of linear response and is characterized by linear dynamic range, in which the responsivity keeps constant. The linear dynamic range and photoresponsivities of the hybrid UV photodetector were characterized by measuring the photocurrent with varying light intensity from 1×10^{-2} to 1×10^{-9} W/cm², as shown in Figure 7 and the inset, respectively. The hybrid photodetector shows a

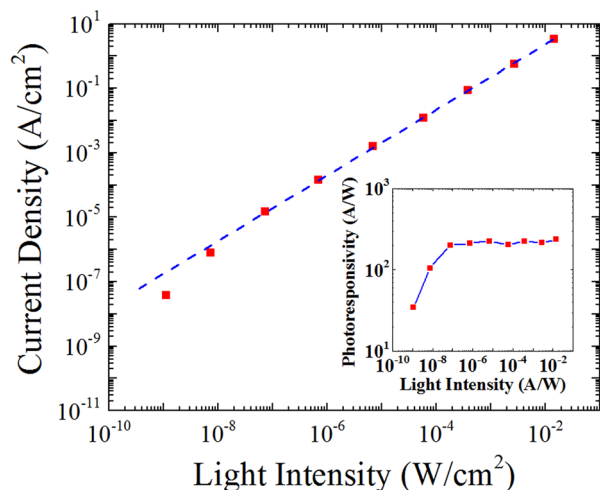


Figure 7. Linear dynamic range of the hybrid UV photodetector. (Inset) Photoresponsivities under different illumination intensities.

linear response within the incident light intensity range from 1×10^{-2} to 1×10^{-8} W/cm², corresponding to a linear dynamic range of ~ 60 dB. This is comparable to those of many inorganic photodetectors, such as GaN (50 dB) and InGaAs (66 dB), but still lower than that of silicon photodetectors (120 dB).^{15,16}

The specific detectivity (D^*) of the photodetector can be expressed by the following formula

$$D^* = \frac{R\sqrt{A \times \Delta f}}{i_n}$$

where the i_n is the noise current in units of A/Hz^{1/2}, Δf is operating bandwidth in hertz, and A is the area of the device in cm².¹⁵ On the assumption that the noise-current is dominated by a shot noise component in the dark current ($i_n = i_{\text{shot}} = (2qi_{\text{dc}}\Delta f)^{1/2}$), D^* can be expressed as^{17,18}

$$D^* = R(A/2qi_{\text{dc}})^{1/2}$$

where q is the electron charge and i_{dc} is the dark current of the device. A specific detectivity of 3.72×10^{14} Jones can be obtained at 351 nm for the photodetector when biased -10 V, which is 2–3 orders of magnitude larger than those of silicon and GaN ultraviolet photodetectors.

Response speed is another important parameter of photodetectors. The transient response of the hybrid photodetector was measured by turning on and off an UV LED with a center peak wavelength at 335 nm, as shown in Figure 8. The rise time (measured from 10% to 90%) and fall time (from 90% to 10%)

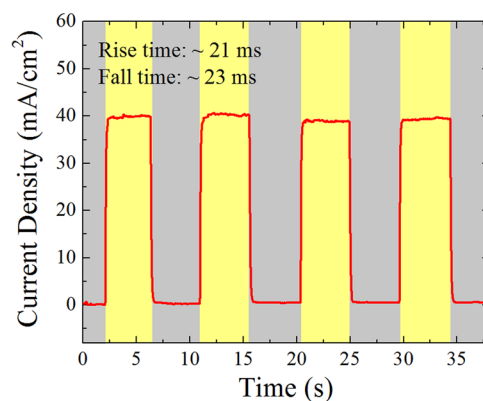


Figure 8. Transient response of the hybrid UV photodetector measured by turning on and off an UV LED with center peak wavelength at 335 nm.

were measured to be around 21 and 23 ms, respectively. This is at least 3 orders of magnitude faster than UV photodetectors that fabricated from wide band gap metal oxides such as ZnO, TiO₂, and WO₃, though they can also achieve high photoresponsivity and high EQE.^{19–21} Such a fast transient response is very desirable for its practical applications in high-frequency or high-speed devices, such as light-wave communications or optoelectronic switches.

Lastly, it is worth mentioning that the conception of the UV photodetector presented in this work can be extended for design and fabrication of many other high-performance UV photodetectors that operate under hole injection mode. For example, we replaced the active layer (mCP–TiO₂ NPs) of the UV photodetector presented in this work with PVK–ZnO NPs or mCP–ZnO NPs composites, and the UV photodetectors with revised structures achieved similar high performance. The photoresponsivity spectra and EQE of the two UV photodetectors are presented in Figure 9. Therefore, it is reasonable

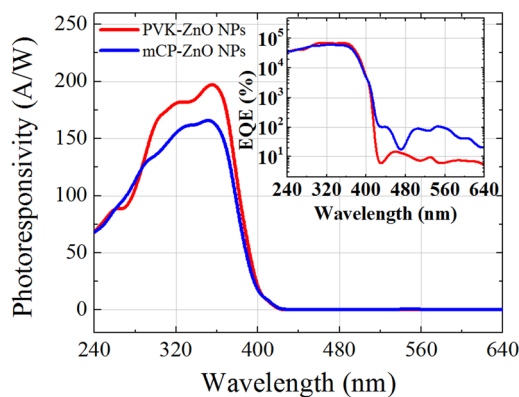


Figure 9. Photoresponsivity spectra of hybrid UV photodetectors using PVK–ZnO NPs or mCP–ZnO NPs composites as active layers. (Inset) Calculated EQE of the two hybrid UV photodetectors.

to conclude that the active layer of the UV photodetectors with hole injection operation mode may be replaced by many other composites consisting of wide band-gap semiconductor NPs and hole conductive polymers, such as PVK–WO₃ NPs, mCP–WO₃ NPs, mCP–SnO₂ NPs, etc.

4. CONCLUSIONS

A novel and high-performance UV photodetector is fabricated by sandwiching a mCP–TiO₂ NPs nanocomposite layer between charge-selective semiconducting polymers. The mCP–TiO₂ NPs nanocomposite layer acts as a “valve” controller that enables hole injection into the device upon UV illumination. The UV photodetector demonstrated a high photocurrent to dark current ratio ($\sim 10^4$), a large linear dynamic range of 60 dB, and a remarkable external quantum efficiency ($\sim 8.5 \times 10^4\%$) for the UV light at 351 nm that is significantly higher than commercial inorganic photodetectors. In addition to the high performance of the UV photodetector, the device structure conception presented in this work may be extended for design and fabrication of many other high-performance UV photodetectors. Further investigation in this route is highly desirable.

AUTHOR INFORMATION

Corresponding Author

*E-mail: sawyes@rpi.edu.

Notes

The authors declare no competing financial interest.

ACKNOWLEDGMENTS

The authors gratefully acknowledge support from National Security Technologies through NSF Industry/University Cooperative Research Center Connection One. The authors also acknowledge the National Science Foundation Smart Lighting Engineering Research Center (EEC-0812056) and a NSF career award (DMR-1151028).

REFERENCES

- (1) Blank, T. V.; Gol'dberg, Y. A. Semiconductor Photoelectric Converters for the Ultraviolet Region of the Spectrum. *Semiconductors* **2003**, *37*, 999–1030.
- (2) Shao, D.; Yu, M.; Lian, J.; Sawyer, S. An Ultraviolet Photodetector Fabricated from WO₃ Nanodiscs/Reduced Graphene Oxide Composite Material. *Nanotechnology* **2013**, *24*, 295701.
- (3) Li, H.-G.; Wu, G.; Shi, M.-M.; Yang, L.-G.; Chen, H.-Z.; Wang, M. ZnO/Poly(9,9-dihexylfluorene) Based Inorganic/Organic Hybrid Ultraviolet Photodetector. *Appl. Phys. Lett.* **2008**, *93*, 153309.
- (4) Jin, Y. Z.; Wang, J. P.; Sun, B. Q.; Blakesley, J. C.; Greenham, N. C. Solution-Processed Ultraviolet Photodetectors Based on Colloidal ZnO Nanoparticles. *Nano Lett.* **2008**, *8*, 1649–1653.
- (5) Guo, F.; Yang, B.; Yuan, Y.; Xiao, Z.; Dong, Q.; Bi, Y.; Huang, J. A Nanocomposite Ultraviolet Photodetector Based on Interfacial Trap-Controlled Charge Injection. *Nat. Nanotechnol.* **2012**, *7*, 798–802.
- (6) Yang, H. Y.; Son, D. I.; Kim, T. W.; Lee, J. M.; Park, W. I. Enhancement of the Photocurrent in Ultraviolet Photodetectors Fabricated Utilizing Hybrid Polymer-ZnO Quantum Dot Nanocomposites Due to an Embedded Graphene Layer. *Org. Electron.* **2010**, *11*, 1313–1317.
- (7) Lin, Y.-Y.; Chen, C.-W.; Yen, W.-C.; Su, W.-F.; Ku, C.-H.; Wu, J.-J. Near-ultraviolet Photodetector Based on Hybrid Polymer/Zinc Oxide Nanorods by Low-Temperature Solution Processes. *Appl. Phys. Lett.* **2008**, *92*, 233301.
- (8) Mondal, R.; Ko, S.; Norton, J. E.; Miyaki, N.; Becerril, H. A.; Verploegen, E.; Toney, M. F.; Brédas, J.-L.; McGeheed, M. D.; Bao, Z. Molecular Design for Improved Photovoltaic Efficiency: Band Gap and Absorption Coefficient Engineering. *J. Mater. Chem.* **2009**, *19*, 7195–7197.
- (9) Roncali, J. Molecular Engineering of the Band Gap of π -Conjugated Systems: Facing Technological Applications. *Macromol. Rapid Commun.* **2007**, *28*, 1761–1775.
- (10) Hou, J.; Park, M.-H.; Zhang, S.; Yao, Y.; Chen, L.-M.; Li, J.-H.; Yang, Y. Bandgap and Molecular Energy Level Control of Conjugated Polymer Photovoltaic Materials Based on Benzo [1,2-b:4,5-b'] Dithiophene. *Macromol. Rapid Commun.* **2008**, *41*, 6012–6018.
- (11) Tseng, Y.-C.; Mane, A. U.; Elam, J. W.; Darling, S. B. Ultrathin Molybdenum Oxide Anode Buffer Layer for Organic Photovoltaic Cells Formed Using Atomic Layer Deposition. *Sol. Energy Mater. Sol. Cells* **2012**, *99*, 235–239.
- (12) Girotto, C.; Voroshazi, E.; Cheyns, D.; Heremans, P.; Rand, B. P. Solution-Processed MoO₃ Thin Films As a Hole-Injection Layer for Organic Solar Cells. *ACS Appl. Mater. Interfaces* **2011**, *3*, 3244–3247.
- (13) Vogel, M.; Doka, S.; Breyer, C.; Lux-Steiner, M. C.; Fostiropoulos, K. On the Function of a Bathocuproine Buffer Layer in Organic Photovoltaic Cells. *Appl. Phys. Lett.* **2006**, *89*, 163501.
- (14) Gommans, H.; Verreert, B.; Rand, B. P.; Muller, R.; Poortmans, J.; Heremans, P.; Genoe, J. On the Role of Bathocuproine in Organic Photovoltaic Cells. *Adv. Funct. Mater.* **2008**, *18*, 3686–3691.
- (15) Khan, M. A.; Kuznia, J.; Olson, D.; Van Hove, J.; Blasingame, M.; Reitz, L. High-Responsivity Photoconductive Ultraviolet Sensors Based on Insulating Single-Crystal GaN Epilayers. *Appl. Phys. Lett.* **1992**, *60*, 2917–2919.
- (16) Gong, X.; Tong, M.; Xia, Y.; Cai, W.; Moon, J. S.; Cao, Y.; Yu, G.; Shieh, C. L.; Nilsson, B.; Heeger, A. J. High-Detectivity Polymer Photodetectors with Spectral Response from 300 to 1450 nm. *Science* **2009**, *325*, 1665–1667.
- (17) Yang, T.; Sun, K.; Liu, X.; Wei, W.; Yu, T.; Gong, X.; Wang, D.; Cao, Y. Zinc Oxide Nanowire As an Electron-Extraction Layer for Broadband Polymer Photodetectors with an Inverted Device Structure. *J. Phys. Chem. C* **2012**, *116*, 13650–13653.
- (18) Soci, C.; Zhang, A.; Xiang, B.; Dayeh, S. A.; Aplin, D. P. R.; Park, J.; Bao, X. Y.; Lo, Y. H.; Wang, D. ZnO Nanowire UV Photodetectors with High Internal Gain. *Nano Lett.* **2007**, *7*, 1003–1009.
- (19) Xing, J.; Wei, H.; Guo, E.-J.; Yang, F. Highly Sensitive Fast-Response UV Photodetectors Based on Epitaxial TiO₂ Films. *J. Phys. D: Appl. Phys.* **2011**, *44*, 375104.
- (20) Huang, K.; Zhang, Q.; Yang, F.; He, D. Ultraviolet Photoconductance of a Single Hexagonal WO₃ Nanowire. *Nano Res.* **2010**, *3*, 281–287.
- (21) Wang, X.; Song, W.; Liu, B.; Chen, G.; Chen, D.; Zhou, C.; Shen, G. High-Performance Organic-Inorganic Hybrid Photodetectors Based on P3HT: CdSe Nanowire Heterojunctions on Rigid and Flexible Substrates. *Adv. Funct. Mater.* **2013**, *23*, 1202–1209.